

# Poly(catecholamine) coating and biofunctionalization of CsPbBr<sub>3</sub> microcrystals

Sangyeon Cho<sup>1,2</sup> and Seok Hyun Yun<sup>\*1,2</sup>

Dr. Sangyeon Cho<sup>1,2</sup>, Prof. Seok Hyun Yun<sup>1,2</sup>

<sup>1</sup> Harvard Medical School and Wellman Center for Photomedicine, Massachusetts General Hospital, Cambridge, Massachusetts, 02139, USA

<sup>2</sup> Harvard-MIT Health Sciences and Technology, Massachusetts Institute of Technology, Cambridge, Massachusetts, 02139, USA

\* syun@hms.harvard.edu

Keywords: lead halide perovskite, core-shell, waterproof, microlaser, biofunctionalization

Lead halide perovskites (LHP) microcrystals are promising materials for various optoelectronic applications. Surface coating on particles is a common strategy to improve their functionality and environmental stability, but LHP is not amenable to most coating chemistries because of its intrinsic weakness against polar solvents. Here, we describe a novel method of synthesizing LHP microcrystals in a super-saturated polar solvent using sonochemistry and applying various functional coatings on individual microcrystals *in situ*. We synthesize cesium lead bromine perovskite (CsPbBr<sub>3</sub>) microparticles capped with organic poly-norepinephrine (pNE) layers. The catechol group of pNE coordinates to bromine-deficient lead atoms, forming a defect-passivating and diffusion-blocking shell. The pNE layer enhances the stability of CsPbBr<sub>3</sub> in water by 2,000-folds, enabling bright luminescence and lasing from single microcrystals in water. Furthermore, the pNE shell permits biofunctionalization with proteins, small molecules, and lipid bilayers. Luminescence from CsPbBr<sub>3</sub> microcrystals is sustained in water over 1 hour and observed in live cells. The functionalization method may enable new applications of LHP particles in water-rich environments.

Lead halide perovskites (LHP), such as CsPbBr<sub>3</sub> and CH<sub>3</sub>NH<sub>3</sub>PbBr<sub>3</sub>, in the form of micro- and nanocrystals have emerged as excellent semiconductor materials for light-emitting diodes<sup>[1,2]</sup> and

photovoltaic devices<sup>[3]</sup>. Furthermore, LHP can be used as a gain material for miniature lasers<sup>[4-9]</sup>. The material gain up to  $4,000\text{ cm}^{-1}$  was reported in bulk-like nanocrystals<sup>[10]</sup>. Lasing from single LHP submicron crystals<sup>[8,9]</sup> has been demonstrated with threshold pump fluences of  $0.2\text{-}1\text{ mJ/cm}^2$ . Such miniaturized and efficient LHP lasers may have potential as life-science tools for cell tagging<sup>[11]</sup>, intracellular sensing<sup>[12]</sup>, and deep-tissue imaging<sup>[7]</sup>, if they can be made stable in the aqueous environment and compatible with biological systems. However, thus far this possibility has been out of the question because of the extreme weakness of LHPs in water.

The poor stability of LHPs in water is intimately related to their ionic nature. Unlike traditional inorganic semiconductors that require high-temperature epitaxial growth, LHPs are solution processable at room temperature. This low lattice energy inevitably leads to low stability in the polar environment. Appropriate encapsulation can protect LHP crystals from reactive molecules, enhancing device stability. However, methods to coat LHP, such as atomic layer deposition (ALD)<sup>[13,14]</sup>, calcination<sup>[15]</sup>, Van der Waals force<sup>[16]</sup>, and sol-gel processes<sup>[17-19]</sup>, have been limited to encapsulating ensembles of, not individual, LHP particles in macroscopic hydrophobic matrices. Furthermore, coating precursors used in these methods cause partial damages to LHPs<sup>[13,15-18]</sup>, and the photoluminescence (PL) properties of LHP can be compromised<sup>[20]</sup>.

Herein, we report novel techniques that enable us to add various protective and functional materials on the surface of inorganic LHP microcrystals. We use organic poly-norepinephrine (pNE) for an initial coating on CsPbBr<sub>3</sub> microcrystals. The pNE polymer layer then allows us to conjugate various biological functional materials via spontaneous reactions at room temperature. We demonstrate core-shell LHP microparticles with 2-fold improved quantum-yield and 2,000-fold improved material stability in water. Functionalized LHP particles internalized by biological cells generate bright luminescence in the cytoplasm.

**Figure 1a** depicts the schematic of our novel core-shell particle synthesis based on sonochemical crystallization of the LHP core and subsequent polymerization of the pNE shell. First, CsBr (75 mM) and PbBr<sub>2</sub> salts (75 mM) are added into N,N-dimethylformamide (DMF) in room temperature. The PbBr<sub>2</sub> salts are partially dissolved in the DMF solution to produce Pb<sup>2+</sup> and Br<sup>-</sup> and the complexation<sup>[21]</sup> of PbBr<sub>3</sub><sup>-</sup> and PbBr<sub>4</sub><sup>2-</sup>. These ions react with undissolved CsBr salts and form a thin layer of orange-color CsPbBr<sub>3</sub> on their surface via fast interfacial reactions (Figure S1a). Ultrasonication is applied to the mixture for about two minutes using a bath- or tip-based ultrasonicator (Figure S1b). Once ultrasonication starts, the remaining salts with interfacial

CsPbBr<sub>3</sub> are broken into smaller pieces by ultrasonic forces and completely dissolved within 30-50 seconds. As the PbBr<sub>4</sub><sup>2-</sup> concentration reaches a critical level over saturation, the nuclei of CsPbBr<sub>3</sub> are spontaneously formed at the vicinity of ultrasonic bubbles and grow to micro- and submicron crystals via: Cs<sup>+</sup>(sol) + PbBr<sub>4</sub><sup>2-</sup>(sol) → CsPbBr<sub>3</sub>(s) + Br<sup>-</sup>(sol). The growth of microcrystals ceases after about 2 minutes of ultrasonication (Figure S1b).

This one-pot synthesis is two-order-of-magnitude faster than the previous surface-initiated growth process<sup>[22]</sup> that required ~ 20 hours to grow crystals to the size of a few μm. Scanning electron microscopy (SEM) of the CsPbBr<sub>3</sub> microcrystals showed cuboidal shapes without any noticeable cracked edges (Figure S1c and d). The addition of a nonionic surfactant, such as polysorbate 80, to the precursor solution resulted in an anisotropic growth of microplates and nanowires without perturbing supersaturation (Figure S1e).

Once the growth of CsPbBr<sub>3</sub> microcrystals is completed, they remain stable under the dynamic equilibrium in the saturated DMF solution. This opens up the opportunity to coat the surface by adding catecholamines. Poly-catecholamine coating, as found in mussel's sticky footage containing dihydroxyphenylalanine (DOPA) and tyrosine, is known for its ability to coat a wide range of materials<sup>[23,24]</sup>. Following the sonochemical synthesis, we added 4 mg/mL of a norepinephrine (NE) bitartrate salt and a pallet of sodium hydroxide (NaOH) into the solution (Figure 1a). After incubating at 50 °C for 1 hour, pNE shells appear on the surface of the individual microcubes and microplates in the solution (Figure 1b). The solution maintains green fluorescence under ultra-violet (UV) light. It is possible to scale up the production of pNE-coated CsPbBr<sub>3</sub> particles simply by increasing the volume of the reactants (Figure 1c). Typically, we obtained about 10<sup>7</sup> microcrystals per ml of DMF.

Energy-dispersive density spectroscopy (EDS), X-ray photoluminescence spectroscopy (XPS), and powder x-ray diffraction (PXRD) confirmed that the lattice sizes and stoichiometry of CsPbBr<sub>3</sub> after the coating were unchanged. The XPS clearly shows the presence of the pNE shell (Figures 1d ). The nitrogen-to-oxygen signal ratio (N/O) was measured to be ~ 0.4, close to the 0.33 ratio of the NE (Figure 1e). PXRD reveals the orthorhombic structure of single-crystalline CsPbBr<sub>3</sub> (space group *Pbnm*, A=8.20 Å, B=8.24 Å, C=11.74 Å) (Figure 1f). Fourier-transform infrared (FTIR) spectroscopy showed absorption peaks at 3000-3500 cm<sup>-1</sup> corresponding to the amine and hydroxyl groups (Figure 1g). The characteristics absorbance peaks of the catechol and indole ring

appeared at  $1514\text{ cm}^{-1}$  (Figure 1g). These functional groups offer binding sites to conjugate biomaterials via Schiff-base reactions and Michael additions.

SEM and TEM images taken at different reaction times provided further insights into the coating process (Figure 2a). After 15 min of polymerization, a 25-60 nm thick, conformal shell appears unevenly on the surface. This morphology is consistent with our expectation that the NE molecules polymerize laterally via oxidative covalent linkage and grow vertically via  $\pi$ - $\pi$  stacking and  $\text{Pb}^{2+}$ -assisted coordination<sup>[24]</sup>. Initially, the thickness of the conformal pNE shell increases linearly with incubation time, but after 30 min it saturates at 40-80 nm depending on the crystallization direction (Figures 2b and 2c). The growth kinetics was analyzed using the sigmoidal equation<sup>[25]</sup>. In the [010] direction, the maximum growth rate was 4.4 nm/min and the thickness of the pNE layer after 30 min was 76 nm. In the [100] direction, the maximum growth rate was 2 nm/min, and the thickness was 41 nm. This asymmetry is attributed to the smaller steric hindrance at the regular octahedral site of the (010) surface compared to the tilted octahedral site of the (110) surface (Figure 2c, inset).

When the polymerization time exceeds 30 min, mesoporous pNE sheets appear outside the conformal pNE shell. SEM and TEM images present that the mesoporous pNE shell consists of multiple sheets grown along the surface normal (Figure 2a). Each sheet is 1 to 2  $\mu\text{m}$  in lateral size and contains numerous nanopores with 20 to 50 nm sizes and pNE aggregates with 3 to 8 nm in diameter (Figure S3). We speculate that these colloidal pNE aggregates are stacked over time forming the supramolecular sheet structure. The mesoporous pNE shell in saturated DMF solution appears transparent. However, when the saturated DMF was dried out, the mesoporous pNE became dark (light-absorbing) (Figure 2d). Re-soaking the particles into saturated DMF solution recovers the transparency of the pNE shell. This reversible effect is due to the swelling property of the mesoporous pNE. DMF molecules intercalated into the pNE layers disrupt the  $\pi$ - $\pi$  or cation- $\pi$  interactions and affect optical absorption<sup>[26]</sup> and average refractive index<sup>[27]</sup> of the pNE organogel.

High-resolution XPS showed that only 4f orbital electrons in the Pb atoms underwent a spectral blue-shift of 0.8 eV and also a broadening of 0.2 eV after coating (Figure 2e and Figure S3). This indicates that the electronegative catechol group with lone pair electrons binds to the electropositive under-coordinated Pb atoms, forming Lewis acid-base adducts. A density functional theory (DFT) simulation suggests that two oxygen atoms in the catechol form a

bidentate binuclear surface complex with the under-coordinated Pb atoms in the (010) surface (Figure 2f), as found in other catechol-metal oxides<sup>[28]</sup>. The binding energy of pNE to the (010) surface (Figure S4a) was calculated to be  $-0.13$  eV, indicating that this process is thermodynamically favored. The DFT calculation of density of states suggests that the Lewis acid-base adduct can remove shallow trap states between the band edges (Figure S4b).

To confirm this passivation effect, we measured photoluminescence (PL). After conformal pNE coating, the absolute PL quantum yield ( $\eta$ ) of CsPbBr<sub>3</sub> microparticles increased from 1.5 to 2.9%, and the PL emission peak wavelength was blue-shifted from 531 to 525 nm (Figure S4c). These changes indicate reduced shallow-trap density by surface defect passivation<sup>[29]</sup>. Under cyclic continuous-wave optical excitation, the PL intensity of uncoated CsPbBr<sub>3</sub> showed hysteresis due to the filling and saturation of carrier trap states<sup>[30]</sup>. The hysteresis was nearly eliminated after coating (Figure 2g). The measured transient PL decay curves (Figure 2h) were fitted to a double-exponential model (Table S1) with two lifetime constants,  $\tau_1$  and  $\tau_2$ , accounting for fast carrier quenching through trap states and slow radiative recombination, respectively<sup>[31]</sup>. Coated CsPbBr<sub>3</sub> particles exhibited  $\tau_1$  of 2 ns and  $\tau_2$  of 12.2 ns, about 2-fold increase compared to uncoated CsPbBr<sub>3</sub> with  $\tau_1$  of 1.3 ns and  $\tau_2$  of 6.2 ns. Cyclic voltammetry (Figure S5) further confirmed the passivation effect of pNE.

Material stability against water was dramatically improved after pNE coating (Figure 3a). When immersed in water, uncoated CsPbBr<sub>3</sub> microparticles dissolve immediately ( $< 0.3$  s). By contrast, coated CsPbBr<sub>3</sub> microparticles maintained optical absorbance and green fluorescence in water for  $\sim 10$  min. This 2,000-fold enhanced material stability enabled us to observe lasing from single core-shell microparticles in water upon optical pumping (480 nm, pulse width: 5 ns) (Figure 3b and S6). The far-field emission pattern of a core-shell CsPbBr<sub>3</sub> particle with a size of 4  $\mu\text{m}$  showed uniform fluorescence below lasing threshold and bright scattering spots above threshold (Figure 3c; see Figure S7 for a 1.5- $\mu\text{m}$ -sized particle and S7b for a 6- $\mu\text{m}$ -sized particle). A narrowband lasing peak at 537 nm is evident, superimposed on a broad fluorescence background (Figure 3d). This laser particle showed a light-in-light-out (L-L) curve with a pump threshold of 0.85 mJ/cm<sup>2</sup>, 3.4 folds higher than the threshold fluence in the air ( $n=1$ ) due to the higher refractive index ( $n=1.33$ ) of the water (Figure S7c). The linewidth narrowing near the threshold is another evidence of lasing (Figure 3e). The narrowest linewidth near the threshold was about 0.5 nm in

FWHM. Lasing in water lasted over about 100 pump pulses at a fluence of  $1 \text{ mJ/cm}^2$ , after which lasing ceased due to the photodegradation of  $\text{CsPbBr}_3$ .

We measured a large number of  $\text{CsPbBr}_3$  particles in the ambient air and found that the pNE coating allowed substantially smaller  $\text{CsPbBr}_3$  microcrystals to reach lasing threshold, compared to uncoated  $\text{CsPbBr}_3$  particles (Figure S8). Furthermore, the pulse-to-pulse intensity variation from the core-shell particles was 6 times smaller than uncoated particles (Figure S8). These enhanced lasing characteristics are due to the defect passivation by pNE coating.

The considerable lifetime ( $>5 \text{ min}$ ) of core-shell laser particles in water allow many spontaneous chemical reactions to be used for surface functionalization. We performed four different proof-of-concept experiments to demonstrate functionalization with biomolecules.

First, we encapsulated core-shell perovskite particles with lipid bilayers (Figure 4a). For this, we prepared  $1\text{-}\mu\text{m}$ -size large unilamellar vesicles (LUVs) made of DIR dye-labeled, 1,2-dioleoyl-sn-glycero-3-phosphoethanolamine (DOPE) and 1,2-dioleoyl-3-trimethylammonium-propane (DOTAP) using a conventional extrusion method<sup>[32]</sup>. When mixed with pNE-coated particles in water, LUVs are deposited on the surface of the pNE via direct vesicle fusion (Figure 4b, inset). The lipid bilayer-functionalized core-shell  $\text{CsPbBr}_3$  microparticles produced PL for over 1 hour in water (Figure 4b). Further improved stability enabled us to deliver the lipid-coated particles to the cytoplasm of 4T1 breast cancer cells *in vitro* (Figure 4c). Upon excitation, distinct green fluorescence is generated from the particles in the cytoplasm.

Secondly, we conjugated biotin-dPEG<sub>23</sub>-NH<sub>2</sub> to the pNE shell using Schiff-base reaction (Figure 4d). The biotinylated LHP particles are firmly anchored on a streptavidin-coated plate (Figure 4e). Under a strong pump fluence ( $2 \text{ mJ/cm}^2$ ), the optical radiation force moves non-biotinylated particles<sup>[33]</sup>, but biotinylated particles remain stationary (Figure 4f).

Thirdly, we functionalized core-shell LHP particles with fluorescent proteins (Figure 4g). DsRed fluorescent proteins (RFPs) in the phosphate buffered saline (PBS) were mixed with pNE-coated  $\text{CsPbBr}_3$  particles in ethanol with 1:1 volume ratio. The mixture was incubated for 5 min for the RFPs to attach to the pNE via Schiff-base reaction. Fluorescence spectroscopy (Figure 4h) and imaging (Figure 4i) confirmed the presence of RFP on the surface of the microparticles. The gradual binding of RFP is evident in the spectral shift of the laser peak and the increase of RFP emission (Figures 4j and S9). It is noteworthy that partial anion exchange chemistry can tune the fluorescence color of LHP particles via solid-state halide diffusion<sup>[34]</sup>. The LHP-protein hybrid

microparticles have potential for biological applications such as multiplexed assay<sup>[35]</sup>, single molecule biophysics<sup>[36]</sup> and hyperspectral imaging<sup>[37]</sup>.

Lastly, we attached bioluminescent Renilla luciferase-8 (Rluc8) on the surface of particles (Figure 4k). Rluc8-coated hybrid particles (a mean size of 4  $\mu\text{m}$ ) on a glass substrate produce bioluminescence centered at 420 nm (Figure 4l) when 10  $\mu\text{l}$  PBS solution of 50  $\mu\text{M}$  of C6-methoxyphenylcoelenterazine (MeO-CTZ) was applied. When excited with continuous-wave laser at 491 nm, the hybrid particles showed bright green fluorescence of CsPbBr<sub>3</sub> (Figure 4l).

It is possible to attach a variety of other functional materials, such as alkanethiol molecules for hydrophobic functionalization in organic solvents (Figure S10), plasmonic nanoparticles for local-field enhancement, and conductive polymers for charge-transfer coupled redox sensor to pNE coated microparticles. As alternatives to polycatechol, self-polymerizable polyethyleneimine<sup>[38]</sup> with multiple nitrogen atoms and polyphenol coating<sup>[39]</sup> may be used for the coating of LHP particles.

In conclusion, we have demonstrated facile sonochemical crystallization, pNE coating, and large-scale synthesis of single core-shell-type CsPbBr<sub>3</sub> microparticles. The pNE shell enhanced optical properties, extended the lifetime of microparticles in water, and provided rich chemical groups to attach various biomaterials. Biofunctionalization of LHP microparticles opens new possibilities for biological applications.

## Supporting Information

Supporting Information is available from the Wiley Online Library or from the author.

## Acknowledgements

The authors thank Dr. Hao Yan for cell experiment and Dr. Soyoung Kim and Prof. Surendranath at MIT for helping electrochemical characterizations. This research was supported in part by the Massachusetts General Hospital Research Scholar Award and National Institutes of Health (grant no. DP1EB024242). S.C. acknowledges the Samsung Scholarship. Part of this work used the facilities in the Center for Materials Science and Engineering at MIT.

## References

- [1] H. Cho, S.-H. Jeong, M.-H. Park, Y.-H. Kim, C. Wolf, C.-L. Lee, J. H. Heo, A.

- Sadhanala, N. Myoung, S. Yoo, *Science* **2015**, *350*, 1222.
- [2] Y. Cao, N. Wang, H. Tian, J. Guo, Y. Wei, H. Chen, Y. Miao, W. Zou, K. Pan, Y. He, *Nature* **2018**, *562*, 249.
- [3] M. A. Green, A. Ho-Baillie, H. J. Snaith, *Nat. Photonics* **2014**, *8*, 506.
- [4] G. Xing, N. Mathews, S. S. Lim, N. Yantara, X. Liu, D. Sabba, M. Grätzel, S. Mhaisalkar, T. C. Sum, *Nat. Mater.* **2014**, *13*, 476.
- [5] Y. Jia, R. A. Kerner, A. J. Grede, B. P. Rand, N. C. Giebink, *Nat. Photonics* **2017**, *11*, 784.
- [6] H. Zhu, Y. Fu, F. Meng, X. Wu, Z. Gong, Q. Ding, M. V Gustafsson, M. T. Trinh, S. Jin, X. Y. Zhu, *Nat. Mater.* **2015**, *14*, 636.
- [7] S. Cho, M. Humar, N. Martino, S. H. Yun, *Phys. Rev. Lett.* **2016**, *117*, 193902.
- [8] E. Tiguntseva, K. Koshelev, A. Furasova, P. Tonkaev, V. Mikhailovskii, E. V Ushakova, D. G. Baranov, T. Shegai, A. A. Zakhidov, Y. Kivshar, *ACS Nano* **2020**, *14*, 8149.
- [9] S. Cho, Y. Yang, M. Soljačić, S. H. Yun, *arXiv Prepr. arXiv2007.09265* **2020**.
- [10] P. Geiregat, J. Maes, K. Chen, E. Drijvers, J. De Roo, J. M. Hodgkiss, Z. Hens, *ACS Nano* **2018**, *12*, 10178.
- [11] N. Martino, S. J. J. Kwok, A. C. Liapis, S. Forward, H. Jang, H.-M. Kim, S. J. Wu, J. Wu, P. H. Dannenberg, S.-J. Jang, Y.-H. Lee, S.-H. Yun, *Nat. Photonics* **2019**, *13*, 720.
- [12] M. Schubert, L. Woolfson, I. R. M. Barnard, A. M. Dorward, B. Casement, A. Morton, G. B. Robertson, P. L. Appleton, G. B. Miles, C. S. Tucker, *Nat. Photonics* **2020**, *14*, 452.
- [13] A. Loiudice, S. Saris, E. Oveisi, D. T. L. Alexander, R. Buonsanti, *Angew. Chemie Int. Ed.* **2017**, *56*, 10696.
- [14] H. Yu, X. Xu, H. Liu, Y. Wan, X. Cheng, J. Chen, Y. Ye, L. Dai, *ACS Nano* **2019**, *14*, 552.
- [15] Z. Li, E. Hofman, J. Li, A. H. Davis, C. Tung, L. Wu, W. Zheng, *Adv. Funct. Mater.* **2018**, *28*, 1704288.
- [16] H. Wu, S. Wang, F. Cao, J. Zhou, Q. Wu, H. Wang, X. Li, L. Yin, X. Yang, *Chem. Mater.* **2019**, *31*, 1936.
- [17] H. Huang, B. Chen, Z. Wang, T. F. Hung, A. S. Sussha, H. Zhong, A. L. Rogach, *Chem. Sci.* **2016**, *7*, 5699.
- [18] S. Huang, Z. Li, L. Kong, N. Zhu, A. Shan, L. Li, *J. Am. Chem. Soc.* **2016**, *138*, 5749.

- [19] S. Li, D. Lei, W. Ren, X. Guo, S. Wu, Y. Zhu, A. L. Rogach, M. Chhowalla, A. K.-Y. Jen, *Nat. Commun.* **2020**, *11*, 1.
- [20] N. Erathodiyil, J. Y. Ying, *Acc. Chem. Res.* **2011**, *44*, 925.
- [21] S. J. Yoon, K. G. Stamplecoskie, P. V Kamat, *J. Phys. Chem. Lett.* **2016**, *7*, 1368.
- [22] Y. Fu, F. Meng, M. B. Rowley, B. J. Thompson, M. J. Shearer, D. Ma, R. J. Hamers, J. C. Wright, S. Jin, *J. Am. Chem. Soc.* **2015**, *137*, 5810.
- [23] H. Lee, S. M. Dellatore, W. M. Miller, P. B. Messersmith, *Science* **2007**, *318*, 426.
- [24] S. Hong, J. Kim, Y. S. Na, J. Park, S. Kim, K. Singha, G. Im, D. Han, W. J. Kim, H. Lee, *Angew. Chemie Int. Ed.* **2013**, *52*, 9187.
- [25] S. I. A. Cohen, M. Vendruscolo, M. E. Welland, C. M. Dobson, E. M. Terentjev, T. P. J. Knowles, *J. Chem. Phys.* **2011**, *135*, 1.
- [26] M. D'Ischia, A. Napolitano, A. Pezzella, P. Meredith, T. Sarna, *Angew. Chemie - Int. Ed.* **2009**, *48*, 3914.
- [27] G. Loget, J. B. Wood, K. Cho, A. R. Halpern, R. M. Corn, *Anal. Chem.* **2013**, *85*, 9991.
- [28] Y. Liu, K. Ai, L. Lu, *Chem. Rev.* **2014**, *114*, 5057.
- [29] S. M. Vorpahl, S. D. Stranks, H. Nagaoka, G. E. Eperon, M. E. Ziffer, H. J. Snaith, D. S. Ginger, *Science* **2015**, *348*, 683.
- [30] Y. Shao, Z. Xiao, C. Bi, Y. Yuan, J. Huang, *Nat. Commun.* **2014**, *5*, 5784.
- [31] H. Zhang, Y. Wu, C. Shen, E. Li, C. Yan, W. Zhang, H. Tian, L. Han, W. Zhu, *Adv. Energy Mater.* **2019**, *9*, 1803573.
- [32] L. A. Morton, J. P. Saludes, H. Yin, *JoVE* **2012**, e4151.
- [33] M. Liu, T. Zentgraf, Y. Liu, G. Bartal, X. Zhang, *Nat. Nanotechnol.* **2010**, *5*, 570.
- [34] L. Dou, M. Lai, C. S. Kley, Y. Yang, C. G. Bischak, D. Zhang, S. W. Eaton, N. S. Ginsberg, P. Yang, *Proc. Natl. Acad. Sci.* **2017**, *114*, 7216.
- [35] S. F. Kingsmore, *Nat. Rev. Drug Discov.* **2006**, *5*, 310.
- [36] T. Ha, P. Tinnefeld, *Annu. Rev. Phys. Chem.* **2012**, *63*.
- [37] S. J. J. Kwok, N. Martino, P. H. Dannenberg, S.-H. Yun, *Light Sci. Appl.* **2019**, *8*, 1.
- [38] T. Xia, M. Kovichich, M. Liong, H. Meng, S. Kabehie, S. George, J. I. Zink, A. E. Nel, *ACS Nano* **2009**, *3*, 3273.
- [39] T. S. Sileika, D. G. Barrett, R. Zhang, K. H. A. Lau, P. B. Messersmith, *Angew. Chemie Int. Ed.* **2013**, *52*, 10766.

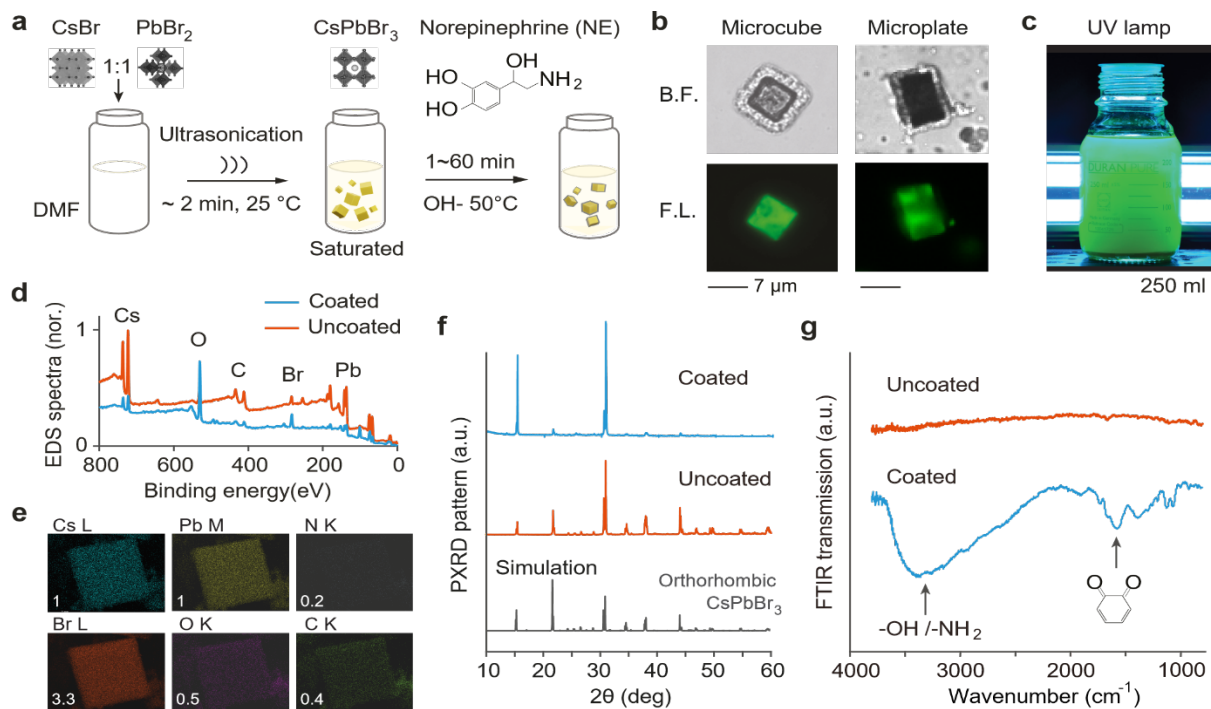


**Figure 1.** One-pot synthesis of core-shell CsPbBr<sub>3</sub>-pNE microcrystals. a) Schematic of two reaction steps: Sonochemistry and polymerization of NE. b) Bright-field (top) and fluorescence (bottom) images of a pNE-coated CsPbBr<sub>3</sub> microcube (left) and microplate (right) in DMF immediately after coating. c) Core-shell particles in DMF under UV lamp. d) XPS spectra of microcrystals with and without pNE coating. e) Spatial elemental maps of a core-shell microparticle for the cesium L line, lead M line, bromine L line, nitrogen K line, carbon K line, and oxygen K line. Numbers are the measured stoichiometry ratio of the Cs, Pb, Br, N, C and O content. f) Measured PXRD patterns of microcrystals with and without pNE coating, in comparison to a simulation result for the orthorhombic structure of CsPbBr<sub>3</sub> (space group Pbnm,  $a = 8.20 \text{ \AA}$ ,  $b = 8.24 \text{ \AA}$ ,  $c = 11.74 \text{ \AA}$ ). g) Absorption spectra of uncoated and pNE-coated microparticles.

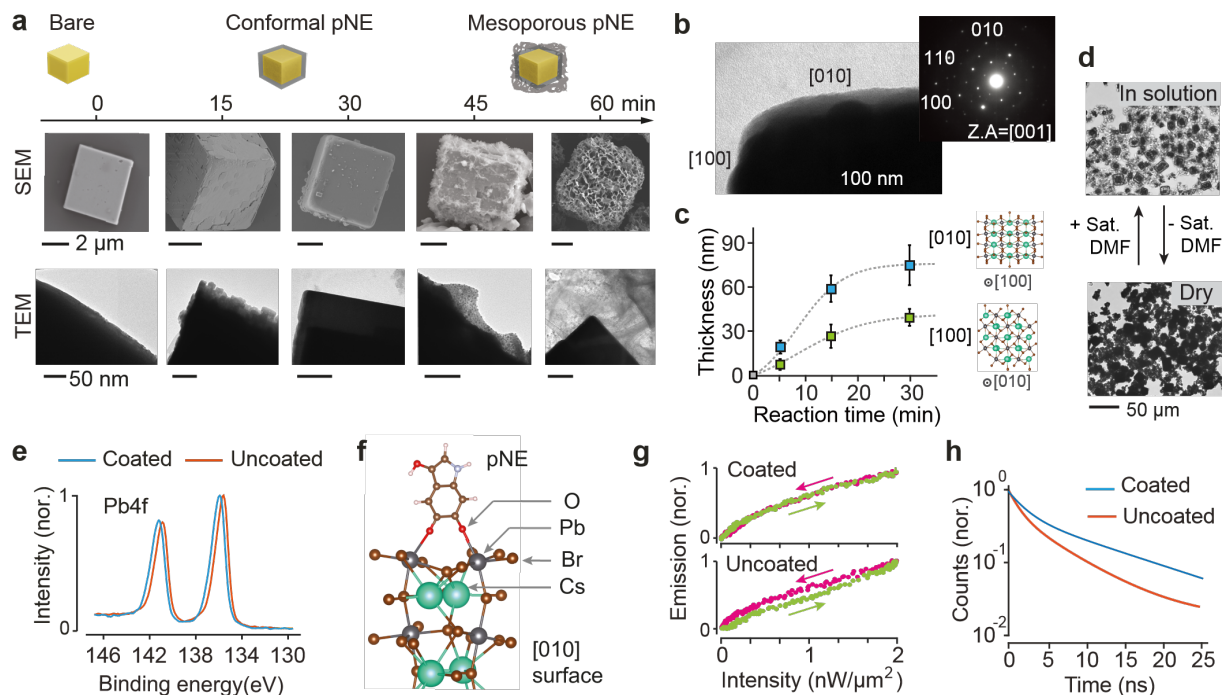


**Figure 2.** Structural and optical characterization. a) Time-lapse SEM and TEM images of different microparticles harvested at different reaction times, and schematic drawings of various reaction intermediates and final products. b) TEM image of the edge of conformal pNE coated CsPbBr<sub>3</sub>. Corresponding selected area diffraction pattern in inset. c) Measured thickness of the thick and thin pNE layers at different reaction times. Dotted lines present sigmoidal fitting. Inset show the atomic structures of the two different planes. d) Optical transmission images of mesoporous pNE coated CsPbBr<sub>3</sub> with and without saturated DMF. e) High-resolution XPS of Pb4f in uncoated and pNE-coated samples. (f) DFT-optimized structure of pNE bound on under-coordinated Pb atoms on the (010) surface of CsPbBr<sub>3</sub>. g) PL curves of bare and coated CsPbBr<sub>3</sub> microparticles upon continuous-wave excitation at 491 nm. h) PL decay of bare and coated microparticles upon picosecond excitation at 382 nm.

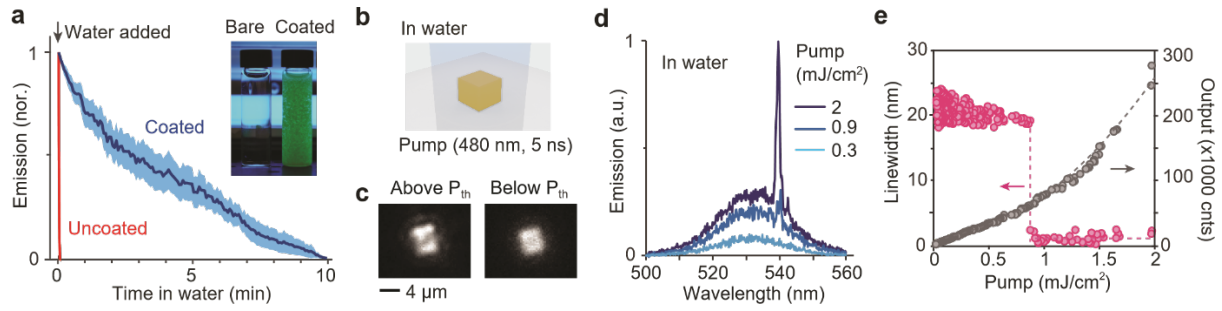


**Figure 3.** Lasing in water. a) Stability of bare and pNE-coated CsPbBr<sub>3</sub> microcrystals in water. The shaded region represents standard deviation of 15 different particles. b) Schematic of optical pumping. c) Emission spectra of a microparticle in water at two different pump fluences. d) Measured spectral linewidth and light-in-light-out curve of a laser particle in water at different pump fluences. A dramatic linewidth reduction occurs at the lasing threshold fluence of 0.85 mJ/cm<sup>2</sup>. e) Emission intensity patterns below and above the threshold for a pNE-coated CsPbBr<sub>3</sub> microcrystal in water.

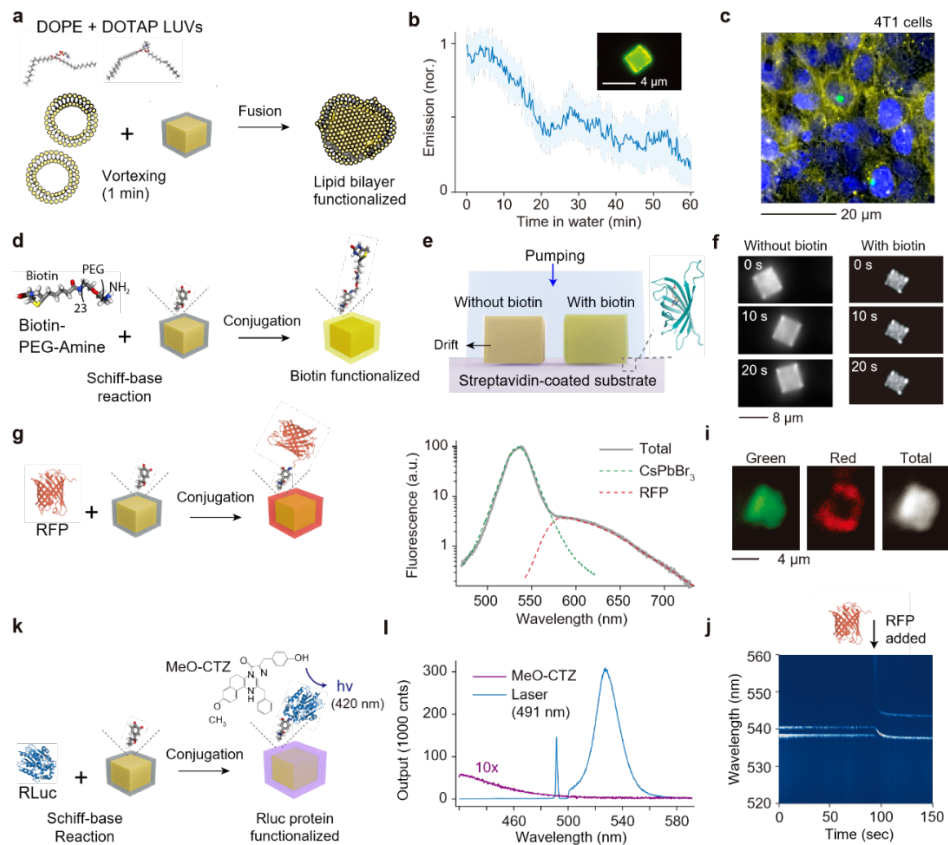


**Figure 4.** Biofunctionalization. a) Schematic of lipid-bilayer functionalization. b) Stability of lipid-coated microcrystals in water. The shaded region depicts the standard deviation of 15 different particles. Inset, image of a single microcube in water emitting green fluorescence from CsPbBr<sub>3</sub> and infrared fluorescence from DIR dye (rendered in yellow) conjugated to the lipid-bilayers. c) Fluorescence image showing the nuclei (DAPI, blue) of 4T1 tumor cells, lipid bilayers (DIR, yellow), and core-shell particles (CsPbBr<sub>3</sub>, green). d) Schematic of biotinylation using biotin-dPEG<sub>20</sub>-NH<sub>2</sub>. e) Schematic of lasing experiment of bare and biotin-functionalized microparticles on the streptavidin coated substrate. f) Time-lapse images showing the immobilization of biotinylated particle due to biotin-streptavidin interaction. g) Schematic of RFP conjugation. h) Emission spectra from a CsPbBr<sub>3</sub>-RFP conjugate particle. i) Fluorescence images of an RFP-coated particle. j) Time-lapse spectroscopy of 1.8 μm-sized laser particle in ethanol. The addition of RFP (10 μM) at 94 s causes a shift of the laser emission wavelength. k) Schematic of bioluminescence protein (RLuc) conjugation. l) Emission spectra from a single RLuc-coated particle. Purple curve: when mixed with MeO-CTZ (in PBS buffer), blue curve: under laser excitation at 491 nm at 1 μW/μm<sup>2</sup>. The peak at 491 nm is due to residual pump light through a dichroic filter.